



Article

Gas-Phase Hydrogenation of Furfural to Furfuryl Alcohol over Cu-ZnO-Al₂O₃ Catalysts Prepared from Layered Double Hydroxides

Guillermo R. Bertolini ¹, Carmen P. Jiménez-Gómez ^{2,*}, Juan Antonio Cecilia ^{2,*} 
and Pedro Maireles-Torres ² 

¹ Centro de Investigación y Desarrollo en Ciencias Aplicadas Dr. J. Ronco CINDECA-CCT La Plata-CONICET-UNLP, Calle 47 N° 257, La Plata 1900, Argentina; bertolg@quimica.unlp.edu.ar

² Departamento de Química Inorgánica, Universidad de Málaga, Cristalografía y Mineralogía (Unidad Asociada al ICP-CSIC), Facultad de Ciencias, Campus de Teatinos, 29071 Málaga, Spain; maireles@uma.es

* Correspondence: carmenpjm@uma.es (C.P.J.-G.); jacecilia@uma.es (J.A.C.); Tel.: +34-952132373

Received: 15 April 2020; Accepted: 27 April 2020; Published: 29 April 2020



Abstract: Several layered double hydroxides (LDHs) with general chemical composition $(\text{Cu,Zn})_{1-x}\text{Al}_x(\text{OH})_2(\text{CO}_3)_{x/2}\cdot m\text{H}_2\text{O}$ have been synthesized by the co-precipitation method, maintaining a $(\text{M}^{2+}/\text{M}^{3+})$ molar ratio of 3, and varying the $\text{Cu}^{2+}/\text{Zn}^{2+}$ molar ratio between 0.2 and 6.0. After calcination and reduction steps, Cu/ZnO/Al₂O₃ catalysts were synthesized. These catalysts were characterized by X-ray diffraction (XRD), transmission electron microscopy (TEM), H₂ thermoprogrammed reduction (H₂-TPR), N₂ adsorption-desorption at −196 °C, N₂O titration, X-ray photoelectron microscopy (XPS), NH₃-thermoprogrammed desorption (NH₃-TPD) and CO₂-thermoprogrammed desorption (CO₂-TPD). The characterization data revealed that these catalysts are mainly meso- and macroporous, where Cu, ZnO and Al₂O₃ are well dispersed. The catalytic results show that these catalysts are active in the gas-phase hydrogenation of furfural, being highly selective to furfuryl alcohol (FOL) and reaching the highest FOL yield for the catalyst with a $\text{Cu}^{2+}/\text{Zn}^{2+}$ molar ratio of 1. In an additional study, the influence of the aging time on the synthesis of the LDHs was also evaluated. The catalytic data revealed that the use of shorter aging time in the formation of the LDH has a beneficial effect on the catalytic behavior, since more disordered structures with a higher amount of available Cu sites is obtained, leading to a higher yield towards FOL (71% after 5 h of time-on-stream at 210 °C).

Keywords: layered double hydroxides; Cu-based catalysts; Cu/ZnO/Al₂O₃; furfural; furfuryl alcohol

1. Introduction

Layered double hydroxides (LDHs), also known as anionic-clays or hydrotalcites, are a group of inorganic lamellar compounds of basic nature. In the last decades, much attention is being paid to the study of these inorganic materials due to their chemical and structural properties, which make them useful in interesting applications, such as adsorbents, catalysts, anion exchangers or flame retardants, among others [1–3]. These materials exhibit high chemical stability, good biocompatibility and pH-dependent solubility [4]. The first LDH reported in the literature, discovered in 1842, was the mineral hydrotalcite $[\text{Mg}_6\text{Al}_2(\text{OH})_{16}]\text{CO}_3\cdot 4\text{H}_2\text{O}$. This inorganic structure results from stacked brucite layers, $\text{Mg}(\text{OH})_2$, where some Mg^{2+} ions can be replaced by Al^{3+} ions, thus generating an excess of positive charge in layers, which must be counterbalanced by the presence of anions, mainly carbonates (CO_3^{2-}), in the interlayer spacing [1–3].

The general formula of LDH is $[M(II)_{1-x}M(III)_x(OH)_2]_x + [A_{n-x/n}]_{x-} \cdot mH_2O$, where M(II) are divalent cations (Mg^{2+} , Zn^{2+} , Cu^{2+} , Ni^{2+}) and M(III) are trivalent cations (Al^{3+} , Fe^{3+} , Cr^{3+}). A^{n-} is an anion of charge n , and m is the stoichiometric value of co-intercalated water [1].

LDHs can be synthesized through several synthesis methods, such as co-precipitation, sol-gel, hydrothermal or urea hydrolysis, although the most usual method is co-precipitation, which can be performed at variable or constant pH [3].

Focusing only on the catalytic properties of LDHs themselves, these inorganic compounds can display both acid and basic sites [5,6]. However, the amount and strength of these acid/basic sites can be modified by thermal treatment, where dehydroxylation and decarbonation processes cause the collapse of the layered structure, leading to the formation of their respective metal oxides [6]. In addition, if any of M(II) or M(III) cations is easily reducible, it is feasible to obtain catalysts with metallic, acid and basic sites, in such a way that they can find a large spectrum of catalytic applications.

Among the great variety of catalytic processes that have emerged in the last century, the biomass valorization to produce high value-added chemicals is attracting the interest of many research groups, as a sustainable alternative to the use of fossil-based raw materials. This great interest has been prompted by the depletion of fossil fuels, which has led to the search and development of alternative sources that can satisfy both chemical and energy demands [7,8]. Biomass is the only feedstock that can replace fossil fuels, but many efforts are still required for the implementation and integration of these processes in the forthcoming biorefineries. However, the selection of a biomass source must be carried out with care and responsibility, since this biomass could interfere with the food chain, causing serious speculation problems and social imbalances. Taking into account these premises, lignocellulosic biomass, coming from agricultural waste, has emerged as an abundant, sustainable and non-edible source of energy, biofuels and chemicals [9]. Lignocellulose is composed by cellulose (40–50%), hemicellulose (20–35%) and lignin (15–25%), which can be extracted selectively by using several thermal, physical and chemical treatments [10].

Focusing only on the hemicellulose fraction, this can be isolated under mild hydrolysis treatment, leading, after depolymerization and hydrolysis, to the respective monosaccharides, mainly xylose [11,12]. Xylose, in turn, can also be dehydrated through homogeneous and/or heterogeneous catalysts to obtain furfural (FUR) as the main product [12,13]. After bioethanol, furfural is the second most produced compound in the sugar platform. The great interest in this organic compound lies in its chemical structure (an aldehyde group and a furan ring with α,β -unsaturations), which confer it a high reactivity [12]. Thus, furfural can be used as feedstock to give rise to a wide range of products with applications in fields, such as polymers, pharmacy, cosmetics, among others, through hydrogenation, oxidation, dehydration, decarbonylation or condensation reactions [12,14,15]. Thus, for instance, different environmentally friendly processes have been reported aimed at the furfural derivatization for the synthesis of valuable chemicals in aqueous media [16,17], as well as in eco-sustainable removable media as deep eutectic solvents, by using homogeneous [18] or heterogeneous catalysts [19,20].

Among the products that can be derived from FUR, furfuryl alcohol (FOL) is the most important. It has been estimated that about 62% of FUR production is employed for the synthesis of FOL due to its importance in resin manufacture for the foundry industry and for chemicals [15]. Industrially, FOL has been synthesized through furfural hydrogenation using a copper chromite catalyst [21–24]. Another product obtained in high proportions during FUR hydrogenation is 2-methylfuran (MF) [12], which is also considered a valuable product as a biofuel additive and for the synthesis of heterocycles [15].

Despite the good performance of the commercial copper chromite catalyst, in the last decade, environmental awareness has led to the search for chromium-free catalysts, which can be more sustainable. As alternative, transition metal-based catalysts, e.g., Cu [25–35], Ni [28,35–41] or Pd [28,42,43] have been proposed to replace copper chromite. Generally, these metals have been dispersed on different supports. Both the hydrogenating character of the metal and the acid/base/redox properties of the support play a determining role in the activity and the product pattern, mainly for those processes where FUR hydrogenation takes place in the gas phase.

In this context, the design of LDHs as catalyst precursors, where some of their cations can be easily reducible, is a suitable approach for the development of active catalysts for FUR hydrogenation to obtain high value-added chemicals. Several authors have reported the synthesis of Ni-based hydrotalcites as efficient catalysts for this reaction, although the high hydrogenating nature of Ni sites [28] leads to a wide range of products, including a high proportion of carbonaceous deposits in many cases [35,36]. A suitable alternative could be the use of Cu-based hydrotalcites, since Cu active centers display a lower hydrogenating capacity, in such a way that the selectivity pattern can be easily controlled. In this sense, previous research has evaluated the role of Al source in the synthesis of Cu/ZnO/Al₂O₃ from their respective hydroxides, after calcination and reduction [44]. These authors achieved well dispersed Cu centers, which were selective towards FOL [44]. In the present work, a series of [CuZn_{1-x}Al_x(OH)₂]_x + [A_{n-x}/n]_x · mH₂O hydrotalcites have been synthesized by coprecipitation method, with different Cu/Zn molar ratio, although the M(II)/M(III) molar ratio (M(II) is Cu(II) + Zn(II)) was 3 in all cases, since this value favors the formation of ordered LDH structures [1–3]. Moreover, the effect of other parameters, like aging time, was also evaluated for the synthesis of LDHs. Precursors were calcined and reduced, and then characterized and tested in the FUR hydrogenation, with special emphasis on the correlation between the amount of available metal sites and their catalytic behavior.

2. Characterization of the Catalysts

The identification of crystalline phases was carried out by powder X-ray diffraction. In all cases, the XRD patterns of LHDs synthesized (Figure 1) are similar to those reported in the literature [1,45]. The most intense peaks correspond to the typical basal (00*l*) planes, thereby, those located at 2θ (°) ≈ 12, 24 and 34 are attributed to the (003), (006) and (009) planes. These can be indexed in a rhombohedral symmetry, which is assigned to a (Cu,Zn)_{1-x}Al_x(OH)₂ (CO₃)_{x/2} m H₂O layered double hydroxide (Powder Diffraction File: PDF: 00-37-0629). In addition, less intense peaks ascribed to non-basal planes of hydrotalcites are also observed, together with other low intense peaks, mainly in those LDHs whose Cu²⁺ or Zn²⁺ content is higher. Thus, in the case of Cu-rich LDH, diffraction peaks attributed to copper(II) hydroxide are presented, while Zn-rich LDH also exhibits broad and poorly defined diffraction peaks attributed to zinc hydroxycarbonate.

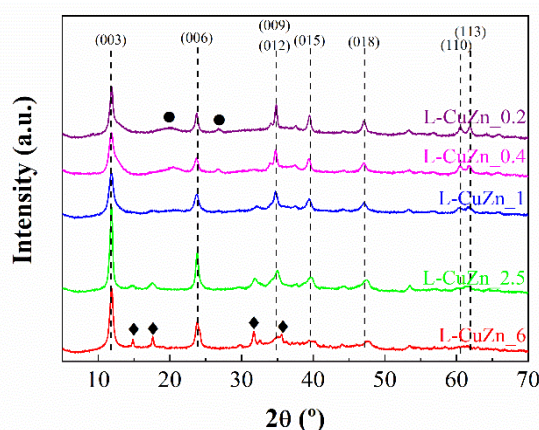


Figure 1. XRD patterns of the layered double CuZnAl hydroxides. (Circles: zinc hydroxycarbonate), (diamonds: copper(II) hydroxide).

CuZnAl-based hydrotalcites have been previously studied by FTIR and Raman spectroscopies, demonstrating that the Cu/Zn molar ratio influences their microstructure. Thus, higher Cu/Zn ratios lead to more homogeneous CuZnAl hydrotalcites, while lower values give rise to less homogeneous structures due to its composition is closer to pure ZnAl and CuAl hydrotalcites [46]. This latter could provoke the asymmetric broadening of Bragg peak profiles of LDH for lower Cu/Zn molar ratio, also characteristic of the stacking disorder for Zn-rich compounds (Figure 1). Moreover, this Raman study

also confirmed the presence of carbonate species, not only as counterion in the interlayer region of LDH, but also in partial segregated malachite for high Cu/Zn molar ratios, which is in agreement with XRD data [46]. Following the procedure described by Santos et al. for $(\text{Cu,Zn})_{1-x}\text{Al}_x(\text{OH})_2(\text{CO}_3)_{x/2}\cdot m\text{H}_2\text{O}$ LDHs [46], these layered materials were thermally treated at 300 °C for 4 h. In their XRD patterns (Figure 2), a broadening of the diffraction peak in comparison to their respective LDHs is noticeable, as a consequence of the stacking disorder of the layered structure due to decarbonation and dehydroxylation of the LDH, leading to the typical diffraction peaks of their mixed metal oxides [1]. Thus, XRD profiles reveal an evolution from the calcined Cu-rich (P-CuZn_6) to the Zn-rich (P-CuZn_0.2) sample. In this sense, the XRD pattern of calcined P-CuZn_6 displays defined bands located at 2θ (°) = 32.5, 35.5, 38.7, 48.8, 53.5, 58.3, 61.6, 66.2 and 68.1 assigned to CuO (PDF: 00-048-1548). The progressive increase in Zn content gives rise to a much more amorphous XRD pattern, being only a broad band observed at 2θ (°) \approx 33. These data suggest that calcined P-CuZn_2.5, P-CuZn_1 and P-CuZn_0.4 display a more amorphous structure, or are formed by smaller particles than that the calcined P-CuZn_6. For the calcined LDH with the highest Zn content (P-CuZn_0.2), broad bands at 2θ (°) = 31.8, 34.4, 36.2, 48.3, 56.5, 63.1 and 68.2, start to emerge. These peaks are assigned to hexagonal ZnO (PDF: 00-36-1451). On the other hand, no diffraction peaks could be ascribed to the presence of crystalline Al species, in such a way that these species must be amorphous, or dispersed in the other phases.

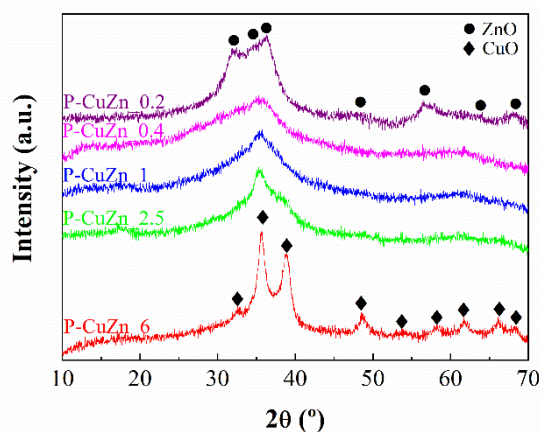


Figure 2. XRD profiles of the mixed oxides obtained after the calcination of LDHs at 300 °C.

Once the catalyst precursors were synthesized after subsequently calcined, H_2 -TPR analysis was carried out to determine the appropriate reduction temperature to obtain the Cu^0 -based catalysts (Figure 3). It has been previously reported that usually it is not possible to discern the different stages of Cu reduction ($\text{Cu}^{2+} \rightarrow \text{Cu}^+ \rightarrow \text{Cu}^0$), so the different contributions observed are ascribed to Cu particles with different size and/or with different interaction with the support ($\text{ZnO}/\text{Al}_2\text{O}_3$) [26,30,34]. From the H_2 -TPR profiles, it can be inferred that the sample with the highest Cu content (CuZn_6) is more easily reducible than the rest of catalysts. Its reduction curve shows two well-defined reduction steps located at 185 and 240 °C, which can be explained by the co-existence of CuO particles with different interaction with the support, or particles with different size. As the Cu content decreases and the Zn content concomitantly increases, the H_2 -TPR profile progressively changes. Thus, it seems clear that the hydrogen consumption at low temperature progressively decreased, as observed for CuZn_2.5 and CuZn_1. In the case of CuZn_0.4, this low temperature band disappears, being only noticeable the presence of a single band whose maximum is located about 245 °C. Those catalysts with a lower proportion of Zn seem to be more reducible than the richer ones, thus indicating that the presence of ZnO would modify the electronic environment around CuO particles, as previously pointed out by other authors [47,48]. Previous research has reported that the reduction of Cu species in CuO/ZnO takes place about 210 °C [30], so Al species could exert an additional electronic promoter effect on the interaction between ZnO and CuO particles, in such a way that the reduction of Cu^{2+} species occurs at

higher temperature, as was indicated in the literature [49]. On the other hand, as the catalyst with a lower Zn content is easily reducible, it is expected that Al species possess a less pronounced promoter effect than ZnO.

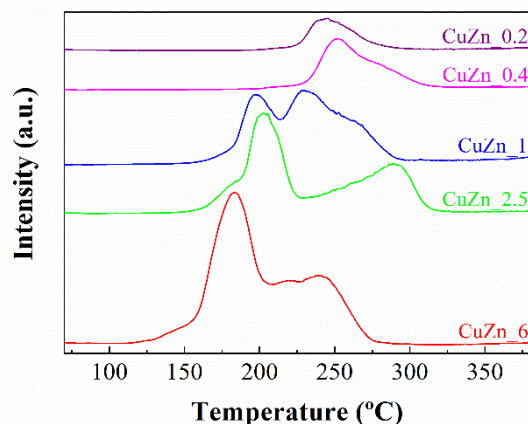


Figure 3. H₂-TPR profiles of the mixed metal oxides obtained after calcination of LDHs.

H₂ consumption data of calcined P-CuZn_X materials are always lower than theoretical values, so a fraction of Cu²⁺ species could not be reduced (Table 1). In this sense, several authors have reported that the reduction of segregated metal carbonates can take place at high temperature, about 550 °C [46]. However, other authors have noted that Cu²⁺ ions could also be embedded in the octahedral sites of Al₂O₃, ZnO, or even ZnAl₂O₄, whose reduction should require a higher temperature [50,51].

Table 1. Chemical composition and H₂ consumption of mixed metal oxides obtained by calcination of LDHs.

Catalyst	Content (wt.%)			Deconvolution H ₂ -TPR (%)		H ₂ Consumption (μmol g ⁻¹)	
	Cu	ZnO	Al ₂ O ₃	Peak 1	Peak 2	Experimental	Theoretical
CuZn_0.2	11.1	71.1	17.8	68	32	1516	1696
CuZn_0.4	19.4	62.3	18.2	59	41	2763	2921
CuZn_1	35.6	45.5	19.0	38	62	4868	5131
CuZn_2.5	53.0	27.2	19.9	5	95	6823	7356
CuZn_6	65.6	14.0	20.5	2	98	8376	8857

Taking into account the H₂-TPR profiles, the precursors were reduced at 300 °C, maintaining this temperature for 1 h to ensure the complete reduction of Cu²⁺ species.

XRD profiles of the CuZn_X catalysts show the typical diffraction peaks of the metallic Cu⁰ at 2θ (°) = 43.3 and 50.4 (PDF: 00-85-1326) (Figure 4). The presence of Cu₂O should be discarded since, despite the main peak at 2θ (°) = 38.3 overlaps with a diffraction peak of ZnO, the secondary peaks of Cu₂O do not appear, so partially reduced copper oxide (Cu₂O) crystallites are not detected, or these are too small to be detected by XRD.

These signals are more defined than those corresponding to the hexagonal ZnO, which does not evolve to reduced Zn species. In the case of Al species, diffractograms do not reveal any characteristic peaks, so these Al species must be highly dispersed in the catalysts. The determination of the crystallite size for Cu⁰ was carried out from the Williamson-Hall equation [52], using the main diffraction peak at 2θ (°) = 43.3. The analysis of this (111) crystallographic plane reveals that the crystallinity of the Cu⁰ particles increases directly with the Cu content, from 5.0 nm for the lowest content (CuZn_0.2) to 28.8 nm for the highest (CuZn_6). These values are slightly lower than those observed for Cu/ZnO or Cu/MgO synthesized by the co-precipitation method [26,30], so Al species, in addition of exerting an electronic promoter effect, seem to favor the dispersion of Cu nanoparticles [49,53].

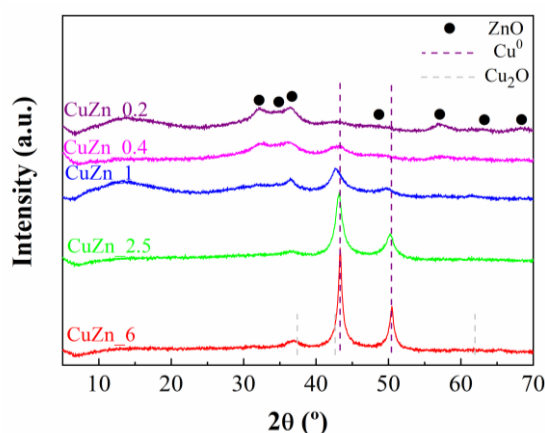


Figure 4. XRD patterns of the CuZn_X catalysts.

In order to elucidate the catalyst morphology, CuZn_X catalysts were analyzed by TEM (Figure 5). In all cases, the micrographs allow to distinguish different morphologies, including layered structures probably due to the hydroxalcite structure that did not fully collapse after the thermal treatment. These data are in agreement with the literature, where a proportion of the layered structure was reported to be maintained after the thermal treatment [54]. In addition, it is noticeable the presence of pseudospherical and well-dispersed nanoparticles, mainly in the samples with a higher Cu content. In both cases, these particles are very small, below 15 nm.

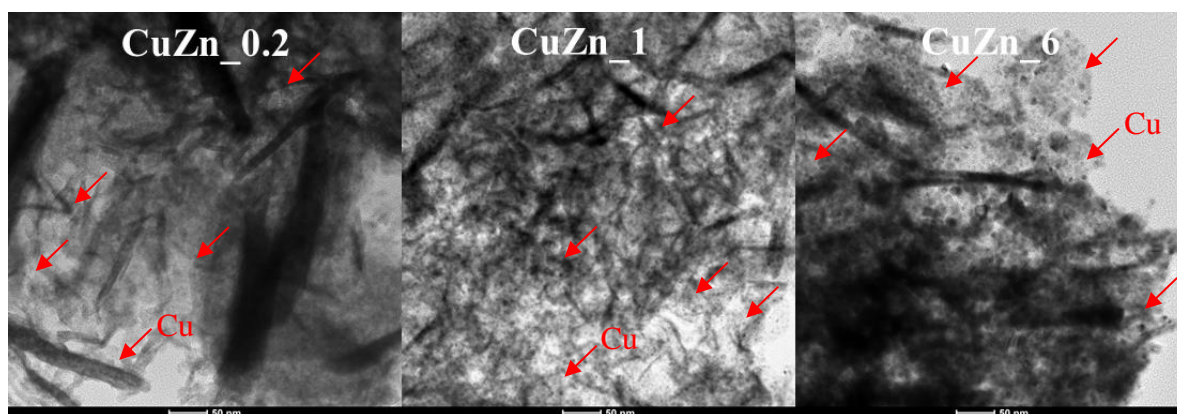


Figure 5. TEM micrographs for CuZn_0.2, CuZn_1 and CuZn_6. (Scale bar: 50 nm).

The analysis of these samples was also performed by Energy Dispersive X-Ray (EDX) (Figure 6). The images show that all elements (Cu, Zn, Al and O) are well dispersed in both lamellar and pseudospherical structures. In Figures 5 and 6, it can be seen the existence of interparticle voids between adjacent nanoparticles.

The textural properties of CuZn_X catalysts were evaluated from their N₂ adsorption-desorption isotherms at −196 °C (Figure 7A). According to the International Union of Pure and Applied Chemistry (IUPAC) classification [55], these isotherms can be considered as Type II, which are typical of macroporous solids, as suggests the great growing of N₂ adsorbed at high relative pressure. The shape is similar for all CuZn_X catalysts, and, consequently, the modification of the Cu/Zn molar ratio does not seem to affect the textural properties of catalysts (Table 2). Thus, S_{BET} values hardly vary, being between 70 and 85 m² g^{−1}, while *t*-plot data indicate that the surface ascribed to the microporosity can be considered as negligible, since values are below 10 m² g^{−1} in all cases. In the same way, the pore volume is very similar for all catalysts, being in the range 0.474–0.679 cm³ g^{−1}, while the micropore volume is very low in comparison to the total volume.

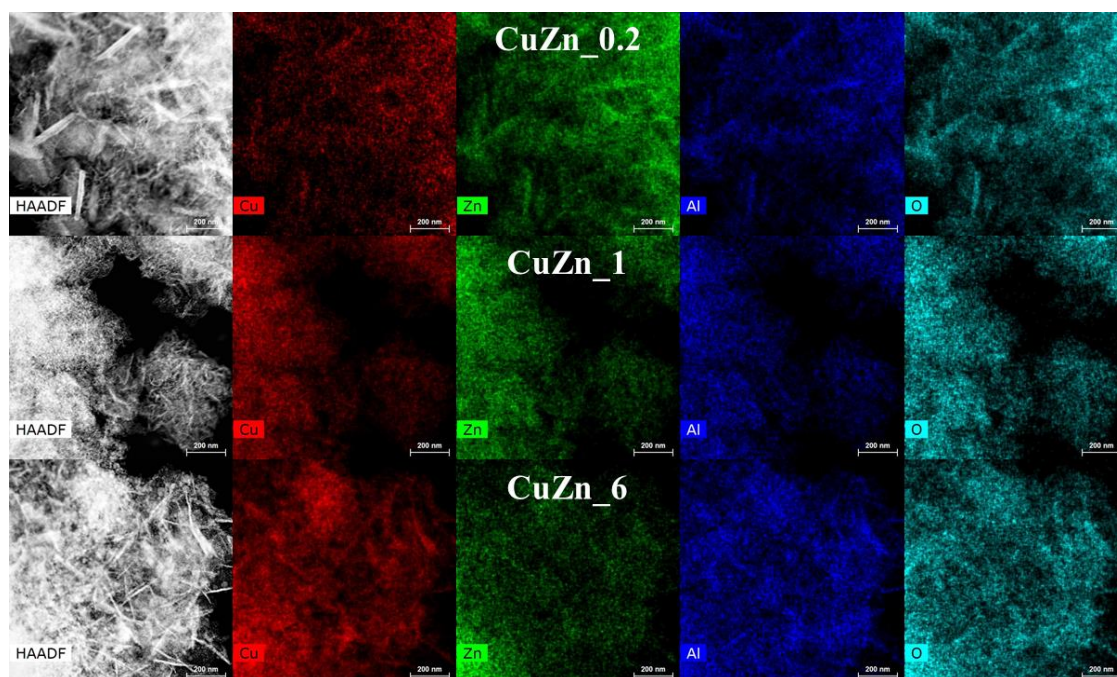


Figure 6. EDX images of CuZn_0.2, CuZn_1 and CuZn_6. (Scale bar: 200 nm).

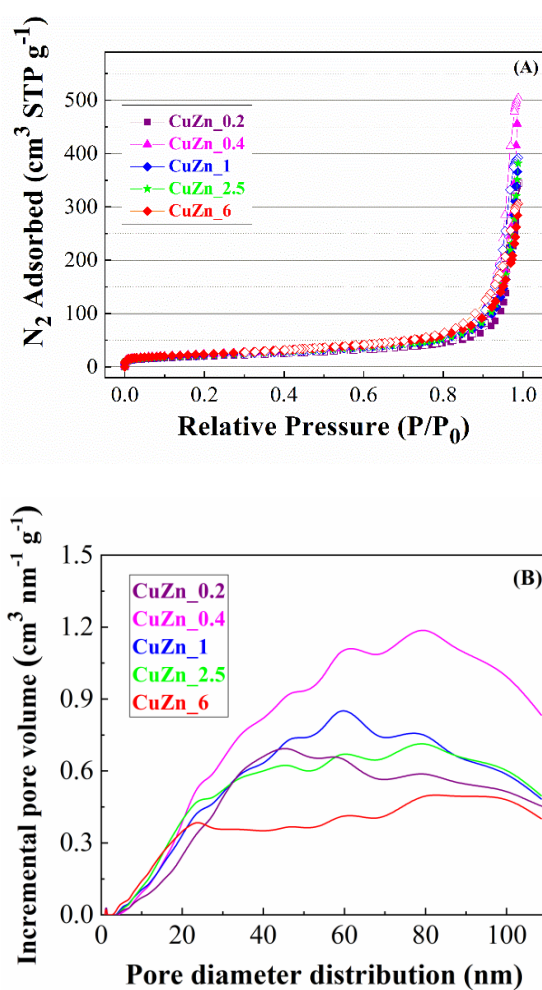


Figure 7. N₂ adsorption-desorption isotherms at -196 °C (A) and pore size distribution estimated by DFT method (B) for CuZn_X catalysts.

Table 2. Textural properties of the CuZn_X catalysts.

Catalyst	S _{BET} (m ² g ⁻¹)	t-Plot (m ² g ⁻¹)	Pore Volume (cm ³ g ⁻¹)	Micropore Volume ¹ (cm ³ g ⁻¹)	Amount Acid Sites ² (μmol g ⁻¹)	Amount Basic Sites ³ (μmol g ⁻¹)
CuZn_0.2	85	5	0.474	0.002	78	39
CuZn_0.4	79	6	0.590	0.003	76	31
CuZn_1	79	1	0.607	0.001	69	22
CuZn_2.5	84	9	0.679	0.005	59	17
CuZn_6	70	8	0.533	0.003	60	15

¹ Micropore volume estimated from alpha-s-plot. ² Quantification of acid sites by NH₃-TPD. ³ Quantification of acid sites by CO₂-TPD.

With regard to the pore size distribution, estimated by Density Functional Theory (DFT) [56] (Figure 7B), all CuZn_X catalysts follow the same pattern. The microporosity is barely appreciated, and only a small contribution appears at 1.2 nm. However, these samples exhibit a wide pore size distribution, extending from 3 to 150 nm, in such a way that these catalysts can be labeled as meso- and mainly macroporous. This porosity is ascribed to the voids between adjacent particles, as was suggested previously from the TEM micrographs (Figures 5 and 6).

The quantification of surface Cu⁰ species of CuZn_X catalysts was carried out by N₂O titration at 60 °C [57] (Table 3). The data indicate that dispersion decreases with the Cu content, going from 21% for CuZn_0.2 to 7% for CuZn_6. In the same way, the metallic surface area (m²_{Cu} g_{Cu}⁻¹) follows a similar trend, and the catalyst with the lowest Cu content (CuZn_0.2) displays the highest value. This study also reveals that the metal particle size increases directly with the Cu loading, from 5 nm for CuZn_0.2 to 19 nm for CuZn_6, being these data slightly lower than those obtained from XRD by using the Williamson-Hall method [52].

Table 3. Metallic properties of CuZn_X catalysts, as determined from N₂O titration.

Catalyst	Superficial H ₂ Uptake (μmol g ⁻¹)	Metallic Surface		Dispersion (%)	Particle Size (nm)	Crystallite Size ¹ (nm)
		(m ² _{Cu} g _{Cu} ⁻¹)	(m ² _{Cu} g _{cat} ⁻¹)			
CuZn_0.2	317	118	13	21	5	5
CuZn_0.4	385	82	16	14	8	6
CuZn_1	475	55	19	10	12	15
CuZn_2.5	563	44	23	8	15	21
CuZn_6	555	35	23	7	19	29

¹ By applying the Williamson-Hall equation to XRD data [52].

In order to determine the surface chemical composition of catalysts, X-ray photoelectron spectroscopy (XPS) analysis was carried out. Cu 2p core level spectra (Figure 8A) show that Cu 2p_{3/2} consists of a single contribution located at 932.0 eV, ascribed to reduced Cu species [30,32], since the absence of the typical shake-up satellite of divalent metals about 942–943 eV would exclude the existence of Cu(II) [58].

However, from this contribution, it is not possible to discern between Cu⁺ and Cu⁰ species, so the Auger Cu_{LMM} signal is used to identify these oxidation states [30,32]. The broad Auger Cu_{LMM} band (Figure 8B) can be deconvoluted in two main contributions: 918.5 eV, which is ascribed to Cu⁰, and 917.0 eV due to Cu⁺ [30]. The proportion of Cu⁰ increases directly with the Cu content, being about 65–70% of the total reduced Cu species. The analysis of the Zn 2p region (Table 4) evidences a single band between 1021.6–1022.1 eV, which is assigned to ZnO. Some studies of Cu/ZnO catalysts have demonstrated that ZnO can be partially reduced, arising a new contribution located at lower binding energy. This new band is not observed in the Zn 2p core level spectra; however, the Auger Zn_{LMM} line (Figure 8C) shows an asymmetric band that would confirm the existence of a small proportion of Zn partially reduced (Zn^{δ+}), or even a synergistic effect between Cu⁰ and ZnO [59,60]. With regard to

the Al 2p core level spectra, all CuZn_X catalysts display a contribution about 74.3 eV, which can be attributed to Al₂O₃ [61]. In the case of O 1s, all catalysts display a main contribution located about 531.0 eV, assigned to oxide species, and another less intense at 532.6 eV, that is assigned to hydroxyl and/or carbonate [61]. The existence of carbonates could be confirmed by the signal at a binding energy of 288–289 eV in the C 1s core level spectra [61], which could result from a low proportion of LDH, or a possible carbonation of the catalyst surface.

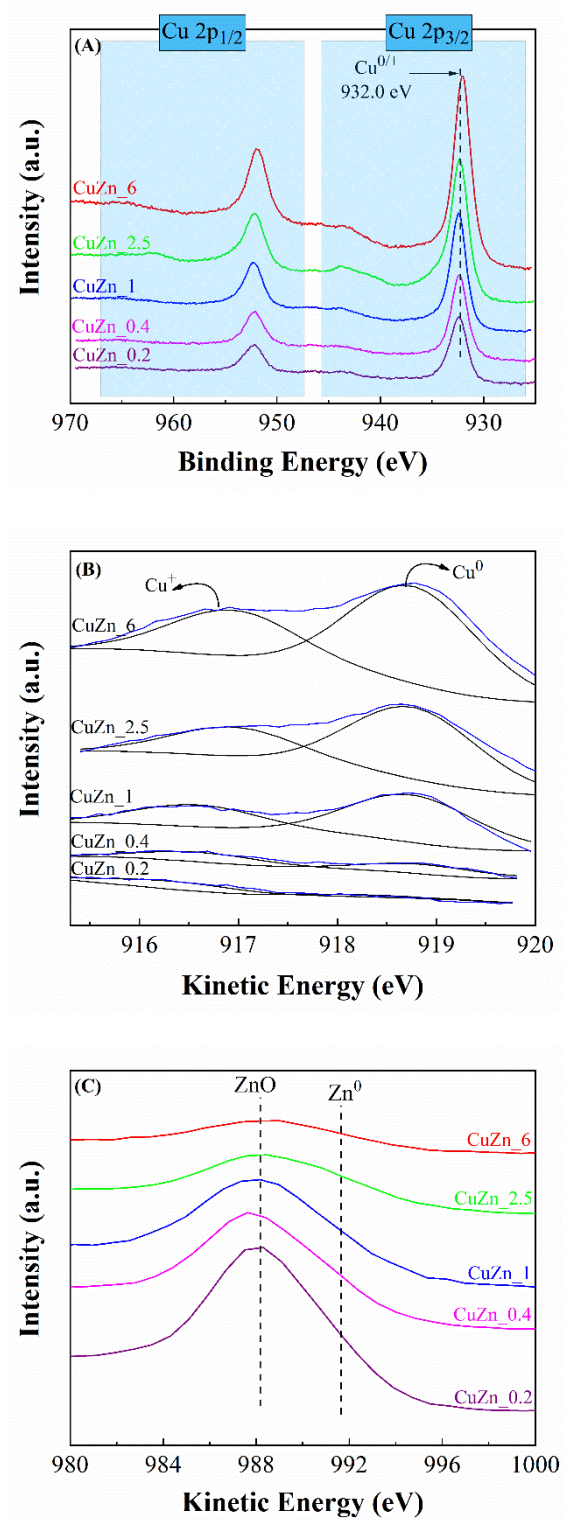


Figure 8. Cu 2p core level (A), Auger Cu_{LMM} (B) and Auger Zn_{LMM} (C) spectra of CuZn_X catalysts.

Table 4. XPS data of CuZn_X catalysts.

Catalyst	Binding Energy, eV (Atomic Concentration, %)						Surface Molar Ratio		
	C 1s		O 1s		Al 2p	Cu 2p	Zn 2p	Cu/Zn	(Cu + Zn)/Al
CuZn_0.2	284.8 (9.6)	288.7 (1.6)	531.1 (46.2)	532.7 (5.8)	74.4 (10.9)	932.0 (3.7)	1022.1 (22.1)	0.15	2.37
CuZn_0.4	284.8 (16.6)	288.8 (0.9)	530.8 (40.7)	532.5 (13.0)	74.3 (9.1)	932.1 (4.5)	1021.9 (15.2)	0.29	2.16
CuZn_1	284.8 (10.1)	288.6 (1.0)	531.0 (38.6)	532.6 (14.1)	74.4 (12.2)	932.1 (8.1)	1022.1 (16.0)	0.51	1.97
CuZn_2.5	284.8 (14.1)	288.4 (0.7)	531.0 (36.7)	532.7 (15.3)	74.5 (11.5)	932.0 (9.8)	1022.1 (11.8)	0.83	1.88
CuZn_6	284.8 (17.4)	288.4 (1.1)	531.0 (37.9)	532.5 (8.7)	74.5 (9.6)	932.0 (11.0)	1021.7 (6.0)	1.83	1.77

The atomic concentration data show that the surface Cu content progressive increases with the Cu loading, as expected (Table 4), although surface molar ratios seem to be lower than the theoretical values. This fact could be ascribed to both ZnO and Al₂O₃ exhibit a smaller crystallite size than Cu⁰, in such a way that both metal oxides should be better dispersed in catalysts. This fact can lead to lower than expected surface Cu concentrations.

As both acid and basic sites could also influence on the gas-phase FUR hydrogenation reaction, NH₃-TPD and CO₂-TPD studies were performed (Table 2). The NH₃-TPD data show a relatively low amount of acid sites, decreasing from 78 μmol g⁻¹ for CuZn_0.2 to 60 μmol g⁻¹ for CuZn_6. The presence of these acid sites is ascribed to Al₂O₃ and Cu⁺, which provide Lewis acid sites, and even to ZnO due to its amphoteric character, similar to alumina. Several authors have reported that the modulation of the acidity plays a key role in FUR conversion, since a high number of acid sites can cause the polymerization of FUR, mainly in gas-phase, leading to the formation of a high proportion of carbonaceous deposits [29,37,62]. These polymerized FUR species interact strongly with the active sites, in such a way that catalysts tend to be deactivated relatively fast. However, the presence of weak acid sites could exert a beneficial effect on the catalytic behavior, since the interaction between FUR, or reaction products, and the catalyst is weakened in comparison with catalyst with higher acidity, thus favoring the desorption of products adsorbed on the catalyst surface. In this sense, several supports, such as SiO₂ or clay minerals, with similar amount of acid sites [29,37], have provided good catalytic activity in FUR hydrogenation, under similar experimental conditions.

Similarly, a basic support (MgO, CaO, ZnO or CeO₂) [25,26,30,63,64] also seems to have a positive effect in this catalytic process. CuZn_X catalysts display a small concentration of basic sites, between 15 and 39 μmol g⁻¹, raising as the Cu content decreases. The presence of these basic sites is ascribed to the amphoteric character of both ZnO and Al₂O₃, as previously mentioned [65,66].

3. Catalytic Results

CuZn_X catalysts were tested in the gas-phase FUR hydrogenation, using FUR dissolved in cyclopentyl methyl ether (CPME). This solvent was selected due to its interesting physico-chemical properties, such as low solubility in H₂O in comparison to other ethereal solvents, low formation of peroxides, low boiling point (106 °C) or relative high stability under acid or basic conditions [67]. Considering these premises, the first study was to evaluate the stability of the solvent under similar experimental conditions to those used for the catalytic evaluation of CuZn_X catalysts. At a reaction temperature of 190 °C, CPME was recovered without any modification, such as the cleavage of the –C–O–C– bond or isomerization.

3.1. Influence of Cu Content

Thereafter, CuZn_X catalysts were studied in the FUR hydrogenation at 190 °C (Figure 9). All the catalysts are prone to suffer a progressive deactivation, which could be a consequence of the strong interaction of FUR, or FOL molecules, with Cu active sites [68]. The catalyst with the lowest Cu content (CuZn_{0.2}) is also the least active catalyst, reaching a FUR conversion of 40% after 1 h of time-on-stream (TOS), which decreases until 26% after 5 h. By increasing the Cu content, the catalytic performance is clearly improved, since CuZn_{0.4} attains a FUR conversion of 43% after 5 h of TOS, while CuZn₁ seems to be the most stable catalyst with a FUR conversion of 59%. However, this trend is not followed when the Cu content raises further, since both CuZn_{2.5} and CuZn₆ catalysts exhibit a similar pattern, reaching a FUR conversion close to 50% after 5 h of TOS.

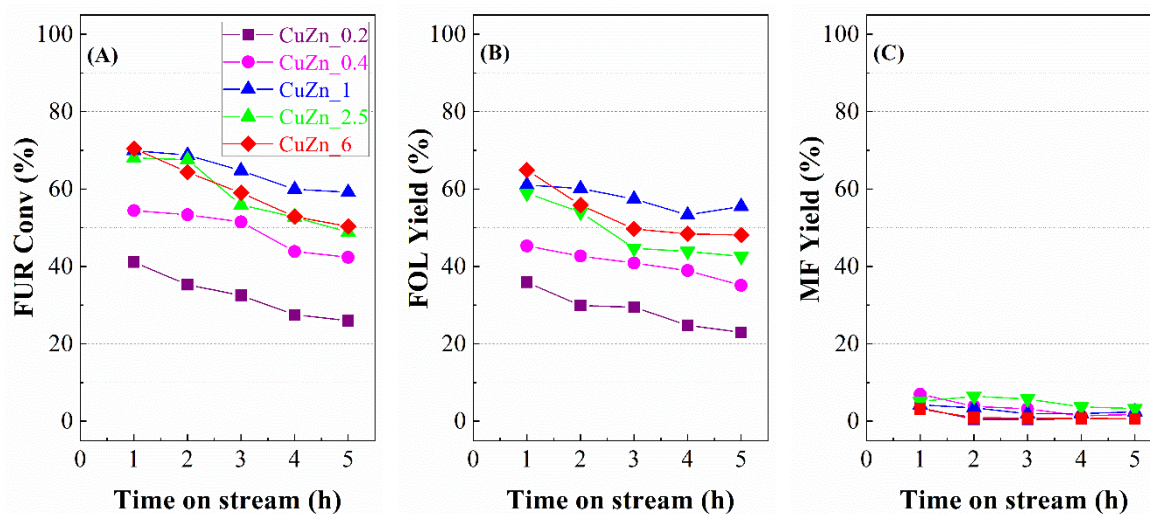


Figure 9. FUR conversion (A), FOL yield (B), and MF yield (C) in the FUR hydrogenation over CuZn_X catalysts (Experimental conditions: Mass of catalyst = 0.15 g, Reaction temperature = 190 °C, Pressure = 0.1 MPa, H₂ flow = 10 mL min⁻¹, Fed flow = 2.3 mmol FUR h⁻¹).

With regards to the selectivity pattern (Figure 9B,C), the modification of the Cu/Zn molar ratio hardly varies the ratio of the obtained products, since FOL always is the main compound, with a maximum yield of 55% for CuZn₁, after 5 h of TOS. In all cases, MF was also detected, although this can be considered a minority because MF yield did not exceed 6% after 5 h of TOS. The catalytic data can be compared with other catalysts reported in the literature. Thus, Cu/ZnO and Cu/CeO₂ catalysts exhibited a high activity in the FUR hydrogenation, but the selectivity pattern is slightly different, since the amount of MF was higher in both cases [30,63]. Other authors have reported that the incorporation of Al₂O₃ exerts a promoter effect in the catalytic behavior due to Al species weaken the Cu-ZnO interaction [44]. This data could be in agreement with those obtained in the H₂-TPR analysis, where the catalyst with a lower ZnO content (CuZn₆) is easily reducible. In earlier studies, Nagajara et al. established that co-precipitation is the most appropriate method to obtain a high dispersion of Cu species on a basic support like MgO [25]. These authors also reached a high activity in FUR conversion, with a high selectivity mainly towards FOL. In the same way, Dong et al. carried out a comparative study with Cu/ZnO, Cu/Al₂O₃ and Cu/SiO₂ [29]. They concluded that the modification of the electronic density in the catalyst due to the Cu-support interaction has a determining role in the catalytic behavior, pointing out that the existence of weak acid sites favors MF formation, mainly in the case of Cu/SiO₂, as a consequence of consecutive reactions (FUR → FOL → MF) [29]. These weak acid sites, associated to both the support and Cu⁺ sites, could be involved in the hydrogenolysis of FOL to MF due to their electron-deficiency [29,69]. Similar results were obtained by Jiménez-Gomez et al., who synthesized Cu/SiO₂ catalyst by a complexation method to disperse Cu species [32]. They observed that, besides the presence of weak acid sites, it is necessary the existence of well-dispersed Cu nanoparticles, since the

electron-deficiency of the catalyst enhanced [29,32]. In the present work, in spite of CuZn_X catalysts have acid sites, the amount of MF can be considered negligible in comparison to data reported in the literature [29,32]. In this sense, the catalysts highly selective towards MF display higher S_{BET} values. This fact supposes a higher FUR-support interaction and consequently a longer residence time, which can favor consecutive reactions. CuZn_X catalysts showed lower S_{BET} values and reduced porosity (Table 2 and Figure 7), mainly ascribed to their meso-macroporous nature. As the pore size is not modulated to the dimensions of the FUR molecule, the interaction FUR-active sites should be weaker, although this fact also has some advantage related to the presence of more labile sites that favor an easier desorption of FUR and products. This trend was also observed for other catalysts synthesized by co-precipitation method, such as Cu/MgO, Cu/ZnO or Cu/CeO₂ [25,30,63]. The existence of Cu⁺ sites, as determined by XPS, does not favor the hydrogenolysis process to form MF, so it could be inferred that textural properties have a more determining role in the hydrogenolysis reaction than the amount of acid sites. However, the hydrogenation FUR → FOL takes place on the metallic sites [28,29] and it does not seem to be affected by the textural properties of catalysts. This fact was confirmed in Cu-based catalysts supported on clay minerals [33,37,70]. Thus, those catalysts with very poor textural properties, like bentonite, or whose pore dimensions hinder the incorporation of Cu nanoparticles, like sepiolite, only dispersed metal nanoparticles on the catalyst surface [33]. In both cases, the catalysts were selective towards FOL. However, the use of a clay mineral with less crystallinity as support led to higher S_{BET} values due to an increase in the micro- and mesoporosity, thus favoring a higher interaction between FUR and the catalyst and longer residence time, in such a way that the reaction can evolve toward consecutive reaction steps [70]. In this sense, the formation of MF is favored by the existence of weak acid sites associated to the aluminosilicate, used as support, (kerolite) and the presence of a small fraction of Cu⁺ species. In these studies, the incorporation of promoters, such as ZnO, MgO or CeO₂, modified the selectivity pattern, with an increase in the FOL yield due to milder interaction between support and Cu species, as indicated their H₂-TPR data [29,37,70], which is in agreement with data reported in the present work.

3.2. Turnover Frequency (TOF)

In order to evaluate the activity of Cu sites, turnover frequency (TOF) data of catalysts were determined. It must be considered that most of catalysts are prone to suffer deactivation by the formation of carbonaceous deposits on the catalyst surface, and consequently the evaluation of the activity of these Cu sites only makes sense at zero time (t_0), as long as these catalysts do not reach a total conversion at t_0 . In this sense, the linearization of the Figure 9A reveals that FUR conversion values vary between 43% for CuZn_0.2 and 76% for CuZn_2.5, at t_0 .

From the extrapolation to t_0 (Figure 10A), it is feasible to determine the corresponding TOF values. The obtained data reveal that CuZn_0.2 displays the lowest TOF (28 h⁻¹), whereas an increase in the Cu content improves TOF, and CuZn_0.4 and CuZn_1 show TOF values of 43 and 44 h⁻¹ respectively. However, the use of larger Cu loadings worsens the efficiency of Cu active sites, since CuZn_2.5 and CuZn_6 reach TOF values of 36 and 37 h⁻¹, respectively. In the same way, from the linearization of the data obtained in Figure 9A, it is possible to evaluate the amount of FUR converted per time unit and mass of catalyst at t_0 (Figure 10B). These data reveal that the highest FUR rate was $1.113 \cdot 10^{-2}$ mmol FUR g⁻¹ h⁻¹ for CuZn_1, while the poorest value was obtained for CuZn_0.2, with a rate of $0.678 \cdot 10^{-2}$ mmol FUR g⁻¹ h⁻¹. In addition, from Figure 10B, an estimation of the catalyst lifetime can be made by extrapolation. These data reveal that the catalyst with longer life is CuZn_1, which could be active for 15.15 h. In this time, the catalyst could convert 0.1537 mmol FUR g⁻¹ before exhaustion.

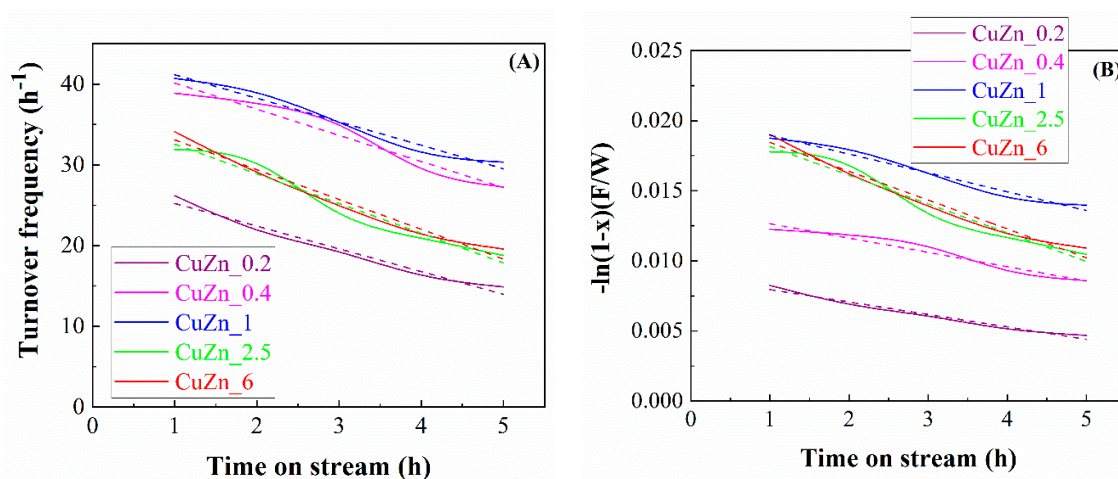


Figure 10. Linearization of TOF values (A) and FUR consumption rate (B) with time-on-stream for CuZn_X catalysts.

3.3. Influence of Reaction Temperature

Considering that CuZn_1 showed the longest lifetime, as well as the most efficient Cu active sites (Table 5), this catalyst was selected to evaluate the influence of the reaction temperature on the catalytic performance (Figure 11). FUR conversion clearly increases with the reaction temperature (Figure 11A), from 34% to 79% after raising the temperature from 170 to 230 °C, after 5 h of TOS. Several authors have reported that FUR hydrogenation is thermodynamically favored; however, the FUR conversion often displays a volcano shape with the reaction temperature, reaching a maximum conversion at 190–210 °C [27,62]. The worsening of the conversion at higher reaction temperature was attributed to FUR polymerization, due to its strong adsorption on the active sites involved in the hydrogenation process. This trend was not observed in the present work, which could be explained by the meso- and macroporosity of catalysts and the relatively low concentration of acid sites, in such a way that the FUR-active site interaction is weaker, so the desorption of FUR and reaction products should be easier [29,37,70]. With regard to the hydrogenation products (Figure 11B,C), in all cases, the main product was FOL, reaching a maximum yield of 65% after 5 h of TOS at 210 °C. MF yield values always were very low, although they increase slightly with the reaction temperature, attaining a maximum MF yield of 7% after 5 h of TOS at 230 °C [62]. Several authors have pointed out that the formation of MF is favored at higher reaction temperature ($T > 190$ °C) [25,30,62]. However, CuZn_1 hardly modifies its selectivity pattern when the reaction temperature increases, probably due to the weaker interaction between the active sites and FUR molecules. Thus, this catalyst seems to be highly stable and selective toward FOL, along the TOS, in a wide range of reaction temperatures [15].

Table 5. Turnover frequency and lifetime analysis of CuZn_X catalysts, obtained from linearization of Figure 10.

Catalyst	TOF ₀ ¹ (h ⁻¹)	C ₀ ² (%)	r ₀ ³ (mmol _{FUR} h ⁻¹ g ⁻¹)	Exhaustion Time ⁴ (h)	Total FUR Converted ⁵ (mmol _{FUR} g ⁻¹)	FUR Converted (1–5 h) ⁶ (mmol _{FUR} g ⁻¹)
CuZn_0.2	28	43	0.6748·10 ⁻²	10.0	0.0440	0.0201
CuZn_0.4	43	58	0.9105·10 ⁻²	13.4	0.0916	0.0307
CuZn_1	44	72	1.1352·10 ⁻²	15.2	0.1537	0.0402
CuZn_2.5	36	76	1.1897·10 ⁻²	9.9	0.0996	0.0366
CuZn_6	37	73	1.1410·10 ⁻²	10.0	0.1021	0.0369

¹ Turnover frequency determined at t₀ (metallic surface data were obtained from Table 3). ² Conversion of FUR at t₀. ³ FUR rates at t₀. ⁴ Total exhaustion time of catalysts. ⁵ Total FUR converted until catalyst exhaustion. ⁶ FUR converted between 1 and 5 h of TOS.

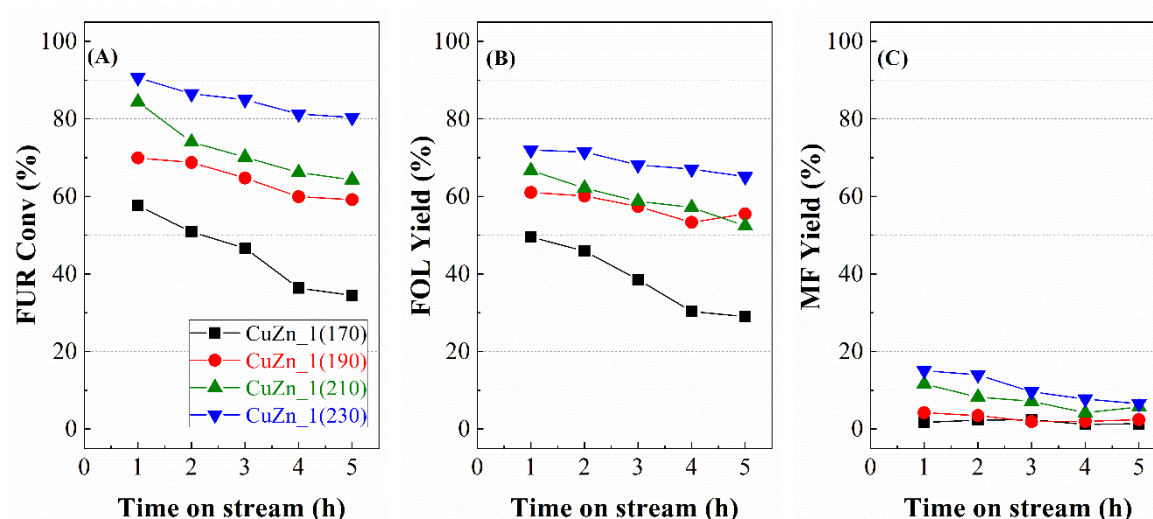


Figure 11. FUR conversion (A), FOL yield (B), and MF yield (C) in the FUR hydrogenation with CuZn₆ (Experimental conditions: Mass of catalyst = 0.15 g, Pressure = 0.1 MPa, H₂ flow = 10 mL min⁻¹, Fed flow = 2.3 mmol FUR h⁻¹).

3.4. Influence of Aging Time in the Synthesis

In the next study, the aging time of the LDHs was modified to evaluate its influence on the catalytic behavior. Thus, three CuZn₁ catalysts with different aging time (1, 48 and 168 h) were compared. The catalytic data show that longer aging time in the synthesis of LDHs has an adverse effect on the catalytic activity (Figure 12A). Thus, that LDH whose aging time was only 1 h gave rise to a catalyst that hardly undergoes deactivation, since it maintains a FUR conversion of 84% after 5 h of TOS at 210 °C. However, a more prolonged aging treatment (168 h) worsens the catalytic activity, achieving a FUR conversion of only 37%, under similar experimental conditions. The selectivity (Figure 12B,C) follows the same trend than that observed previously for CuZn_X catalysts, since FOL was the main product in all cases, attaining a maximum yield of 71%, after 5 h of TOS at 210 °C, with CuZn₁ aged for 1 h. The amount of MF was very low in all cases, although a decrease in MF yield took place as aging time was increased.

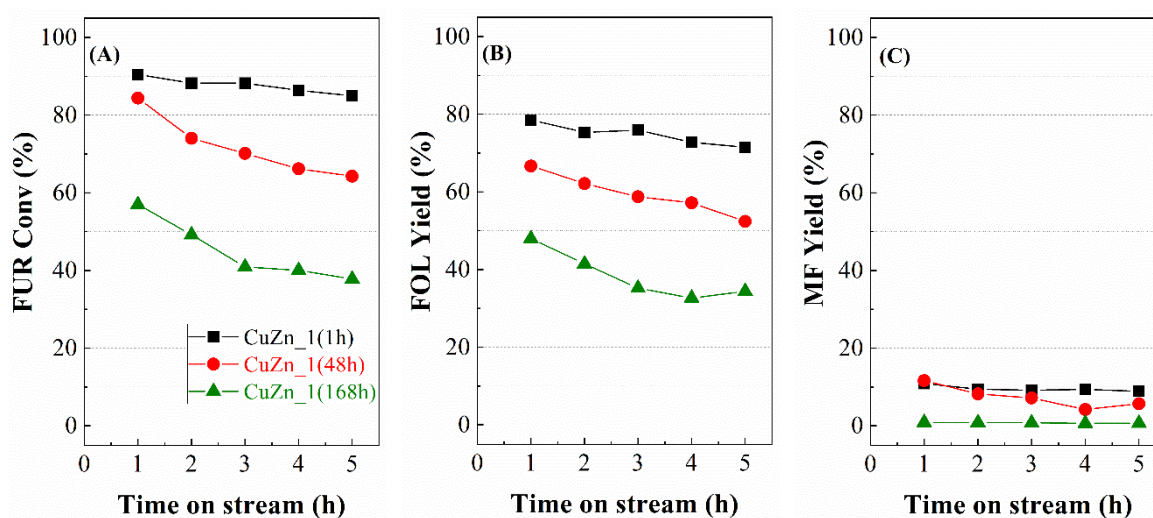


Figure 12. FUR conversion (A), FOL yield (B), and MF yield (C) in the FUR hydrogenation over CuZn₁ catalysts synthesized with different aging time (1–168 h) (Experimental conditions: Mass of catalyst = 0.15 g, Pressure = 0.1 MPa, H₂ flow = 10 mL min⁻¹, Fed flow = 2.3 mmol FUR h⁻¹).

In order to understand the changes of the catalytic behavior for the CuZn_1 catalysts synthesized with different aging times, these catalysts were characterized. Their XRD patterns show clear differences in crystallinity (Figure 13A). Thus, the diffractogram of sample prepared with the shortest aging time (CuZn_1(1h)) does not display any diffraction peak, which are clearly visible for catalysts obtained by increasing the aging time. Thus, CuZn_1(168h) catalyst shows Cu crystallites of 33 nm. These data are in agreement with the literature, since the use of higher temperature and longer aging time favor the growing and better crystallization of layered double hydroxides [3,71]. This fact implies the formation of catalysts where nanoparticles of support and active phase are larger.

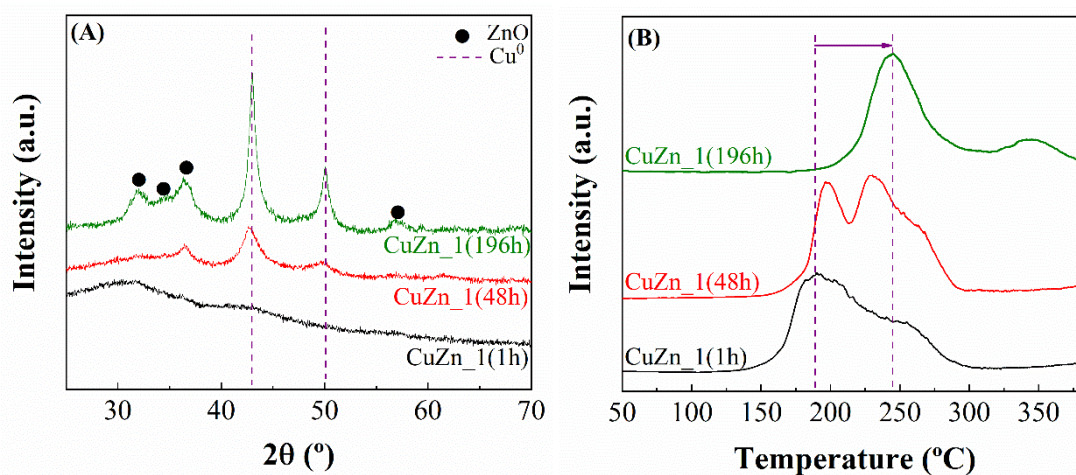


Figure 13. XRD (A) and H₂-TPR (B) profiles of CuZn₁ catalysts synthesized with different aging time.

The analysis of the H₂-TPR profiles also reveals clear modifications depending on the aging time (Figure 13B). Considering that the three catalysts display the same chemical composition, it is expected that the profile differences should be attributable to differences in the size of their Cu nanoparticles. In this sense, a catalyst whose Cu crystallite sizes are smaller (CuZn_1(1h)) is more easily reducible than those catalysts with bigger sizes, as a consequence of the weaker interaction between small CuO nanoparticles and the ZnO/Al₂O₃ support.

In addition, it is also noticeable that both CuZn_1(1h) and CuZn_1(48 h) catalysts display two defined peaks, which could point out the formation of Cu nanoparticles with two different sizes. However, CuZn_1(196h) only shows a peak at higher temperature. This fact could be ascribed to the use of longer aging time, which favors the formation of more homogenous structures. N₂O titration data (Table 6) follow the trend observed by XRD and H₂-TPR, since the catalyst with the lowest aging time (CuZn_1(1h)) is also the catalyst with a higher amount of available surface Cu sites. This would confirm the formation of smaller particles and consequently a higher metallic surface area is obtained, which is in agreement with its better catalytic performance.

Table 6. Metallic characteristic of CuZn₁ catalysts synthesized with different aging time. determined from N₂O titration.

Catalyst	Superficial H ₂ -Uptake ($\mu\text{mol g}^{-1}$)	Metallic Surface		D ¹ (%)	Particle Size (nm)	Crystal Size ² (nm)
		($\text{m}^2_{\text{Cu}} \text{g}_{\text{Cu}}^{-1}$)	($\text{m}^2_{\text{Cu}} \text{g}_{\text{cat}}^{-1}$)			
CuZn_1(1h)	595	69	24	12	9	-
CuZn_1(48h)	475	55	19	10	12	15
CuZn_1(168h)	307	36	12	6	19	33

¹ Copper dispersion. ² Crystal size estimated by Williamson-Hall equation from XRD data [52].

Finally, the superficial analysis of these catalysts by XPS (Table 7) does not reveal any variation in core level spectra in comparison to CuZn_X catalysts. It is only noteworthy a decrease in the surface

Cu content with the aging time, which can be explained by the formation of larger Cu nanoparticles, thus limiting the amount of Cu detected by XPS due to this technique only allows to analyze 2–3 nm of depth (Table 6). With regard to the oxidation state of Cu species, Cu⁰ is the main oxidation state, about a 70–75% of the total Cu, while the Cu⁺ is about 25–30%.

Table 7. Surface atomic concentration of CuZn_1 catalysts synthesized with different aging time.

Catalyst	Atomic Concentration (%)				
	C 1s	O 1s	Al 2p	Cu 2p	Zn 2p
CuZn_1(1h)	11.01	52.83	11.95	8.35	15.86
CuZn_1(48h)	11.06	52.71	12.21	8.07	15.99
CuZn_1(196h)	15.46	50.70	10.87	6.71	16.26

4. Materials and Methods

4.1. Preparation of Catalysts

A series of Cu/ZnO/Al₂O₃ catalysts has been synthesized by co-precipitation method, according to the methodology described by Santos et al. [46]. The LDH precursors were synthesized from aqueous solutions of Cu(NO₃)₂·2H₂O (99%, Aldrich, Saint Louis, MI, USA), Zn(NO₃)₂·6H₂O (99%, Aldrich) and Al(NO₃)₃·9H₂O (99%, Aldrich) with a total metal concentration of 0.3 M. In all cases, (Cu²⁺+Zn²⁺)/Al³⁺ molar ratio was 3, whereas the Cu²⁺/Zn²⁺ molar ratio was varied between 0.2 and 6. In the next step, an aqueous solution of Na₂CO₃ (1.0 M) was slowly added to precipitate metal hydroxides and form the LDH structure. Later, the obtained gel was aged at room temperature for 48 h (in two different synthesis, the gel was aged 1 and 168 h). The obtained solid was filtered and washed with distilled water until reach a neutral pH to ensure the total removal of Na⁺ ions. Finally, the solid was dried overnight at 90 °C and calcined at 300 °C for 4 h, using a ramp of 10 °C min⁻¹.

4.2. Characterization of Catalysts

An X'Pert Pro automated diffractometer (PANalytical, Bruker, Rheinstetten, Germany) was used to obtain powder X-ray diffraction patterns, this equipment are composed of a Ge (111) primary monochromator (Cu Kα1) and a X'Celerator detector with a step size of 0.017° (2θ), between 2θ = 10° and 70° with an equivalent counting time of 712 s per step. Williamson-Hall Equation (1) [52] was applied to calculate the crystallite size (D):

$$B \cos \theta = (K\lambda/D) + (2 \varepsilon \sin \theta) \quad (1)$$

where B is the full width at half maximum (FWHM) of the XRD peaks, θ the Bragg angle, B is, K is the Scherrer constant, λ is the wavelength of the X ray and ε is the lattice strain.

A FEI Talos F200X (Thermo Fisher Scientific, Waltham, MA, USA) system was used to study the catalyst morphology by transmission electron microscopy (TEM). The images obtained with this technique show a high resolution; moreover, this equipment allows the combination of STEM and TEM imaging and, therefore, a 3D characterization with chemical composition mapping. The samples were dispersed in isopropyl alcohol and each one of them was put on a carbon grid.

The temperature of catalysts reduction was evaluated by H₂-TPR (hydrogen temperature-programmed reduction). To carry out the experiments, 0.080 g of sample has been used. First, the catalyst precursor is treated under a He flow (35 mL min⁻¹) at 100 °C for 30 min, after this, it is cooling to room temperature to start the analysis, where the H₂ consumption is monitored between 50 and 800 °C, by using an Ar/H₂ flow (48 mL min⁻¹, 10 vol.% H₂) with a heating rate of 10 °C min⁻¹. An on-line thermal conductivity detector (TCD) (Shimadzu, Kyoto, Japan) was used to carry out the H₂ quantification. It is necessary to trap the water formed in the process to avoid equipment contamination,

so the outcoming flow is passed through a cold finger immersed in a liquid N₂/isopropanol bath (−80 °C).

In previous research [30,37], N₂O titration has been employed to determine the metallic surface area and the dispersion of Cu⁰ species, where the superficial oxidation of Cu⁰ under a N₂O flow takes place according to the Equation (2):



Prior to the analysis, the catalyst precursor was treated under a He flow (35 mL min^{−1}) at 100 °C for 30 min, followed by a reduction step under a 10 vol.% H₂/Ar-flow (48 mL min^{−1}) at 300 °C for 1 h, with a heating rate of 5 °C min^{−1}, being monitored the H₂ consumption by TCD. When the catalyst was reduced, it was cooled until 60 °C under a He flow to carry out the Cu⁰ oxidation to Cu⁺ performed by titration N₂O (5 vol.% N₂O/He), at 60 °C for 1 h. At last, a second sample reduction was carried out by heating from room temperature to 300 °C with a heating rate of 5 °C min^{−1}, being also monitored its H₂ consumption by TCD.

The textural parameters were determined from the N₂ adsorption-desorption isotherms at −196 °C by using an automatic ASAP 2020 Micromeritics apparatus (Micromeritics, Norcross, GA, USA). The sample was previously outgassed at 200 °C and 10^{−4} mbar for 12 h. The Brunauer-Emmet-Teller (BET) equation [72] was utilized to determine surface area taking a N₂ cross section of 16.2 Å². Micropore volume was determined from alpha-s- method. Pore size distribution was determined using the density functional theory (DFT) [56].

X-ray photoelectron spectra were obtained using a Physical Electronic PHI 5700 spectrometer (Physical Electronics, Eden Prairie, MN, USA), equipped with an Electronics 80-365B multichannel hemispherical electron analyzer and an Mg Kα X-ray excitation source (300 W, 15 kV, hv = 1253.6 eV). High-resolution spectra were recorded by a concentric hemispherical analyzer in a 29.35 eV constant energy mode, using a 720 μm diameter analysis area, and the pressure in the analysis chamber was kept below 5 × 10^{−6} Pa. Binding energies (BE) were determined to an accuracy of ± 0.1 eV, using the adventitious carbon C 1s signal at 284.8 eV as reference. PHI ACCESS ESCA-F V6 software (Eden Prairie, Minnesota, USA) was used for data acquisition and analysis. A Shirley-type background was subtracted from the signals. The recorded spectra were always analyzed with Gauss-Lorentz curves, in order to determine more precisely the binding energy of the atomic levels of the different elements. To avoid sample oxidation after reduction, they were stored in sealed vials with an inert solvent; moreover, samples were prepared in a dry box under a N₂ flow, where the solvent was evaporated prior to its introduction into the analysis chamber, and directly analyzed without previous treatment.

To calculate the total acid sites present in the samples, thermo-programmed desorption of ammonia (NH₃-TPD) was carried out. In a typical procedure, 0.08 g of catalyst is placed in a U-shape quartz reactor and cleaned flowing He (40 mL·min^{−1}) up to 400 °C with a heating rate of 10 °C·min^{−1}. Then, the sample is cooled until 100 °C under the same He flow, and once the temperature is stabilized at 100 °C, the sample is saturated with ammonia for 5 minutes and then physisorbed NH₃ was removed under He. Ammonia desorption is performed by heating the sample from 100 to 400 °C, with a rate of 10 °C·min^{−1}, registering the signal using a GC-14B instrument (Shimadzu, Kyoto, Japan) equipped with a thermal conductivity detector (TCD), previously calibrated with Ni(NH₃)₆Cl₂ (Aldrich) in order to quantify total acid sites.

Thermo-programmed desorption of CO₂ (CO₂-TPD) was employed for the quantification of basic sites. In a typical procedure, 0.03 g of catalyst is pretreated under a He flow (40 mL min^{−1}) at 400 °C for 15 min (10 °C·min^{−1}). Later, the sample was cooled to 100 °C and a pure CO₂ stream (60 mL min^{−1}) was subsequently introduced into the reactor for 30 min. Finally, the amount of CO₂ evolved was analyzed using a TCD detector between 100 and 600 °C and a helium flow (10 °C min^{−1}).

4.3. Catalytic Tests

The furfural hydrogenation was carried out at atmospheric pressure in a tubular quartz reactor with an internal diameter of 6.35 mm. For this, 150 mg of pelletized catalyst (325–400 μm) were placed inside the reactor between two layers of quartz wool, which is placed inside a programmable temperature tubular furnace, controlled with a thermocouple. Before starting the reaction, catalysts were reduced in-situ with a hydrogen flow (99.99%, Airgas, Paris, France) of 60 mL min^{-1} for 1 h at the reduction temperature deduced from their corresponding H_2 -TPR profiles (350 $^\circ\text{C}$). Subsequently, the desired reaction temperature is set and once the system is stable, the reaction is carried out under a flow of H_2 that ranges between 10 and 60 ml min^{-1} and a feed flow of 3.87 mL h^{-1} of a furfural solution in cyclopentyl methyl ether (CPME, 5 vol.%), which is introduced with the help of an HPLC piston pump, model 307 SC-10 (Gilson, Middleton, WI, USA).

To avoid problems, such as blockage of the lines in the equipment, furfural was dissolved in cyclopentyl methyl ether (CPME). This solvent is environmentally friendly and has been used in different organic reactions [30]. Reaction samples were collected every hour, dissolved with a chloroform and o-xylene solution (internal standard), stored in sealed vials to be subsequently analyzed by gas chromatography, using a Shimadzu GB-14A chromatograph equipped with a flame ionization detector and a CP-Wax 52 CB capillary column.

In a preliminary test, the CuZn₁ catalyst was chosen to evaluate the stability of this solvent at 190 $^\circ\text{C}$, after 5 h of time-on-stream (TOS), but in the absence of furfural. The analysis of the collected samples confirmed the full recovery of CPME; without any products different from this ether, thus demonstrating its stability. The conversion, selectivity and yield values were determined using the following expressions:

$$\text{Conversion (\%)} = \frac{\text{mol of furfural converted}}{\text{mol of furfural fed}} \times 100 \quad (3)$$

$$\text{Selectivity (\%)} = \frac{\text{mol of the product}}{\text{mol of furfural converted}} \times 100 \quad (4)$$

$$\text{Yield (\%)} = \frac{\text{mol of the product}}{\text{mol of furfural fed}} \times 100 \quad (5)$$

The turnover frequency was calculated as follows (6):

$$\text{TOF} = -\frac{\ln(1-X)}{\left(\frac{W}{F}\right) \times M} \quad (6)$$

where F is the molar rate of furfural (mol h^{-1}), W is the catalyst weight (g), X is the conversion and M is the mole of sites loaded (mol g^{-1}). This equation, in which $-\ln(1-X)$ substitutes for X assumes a pseudo first-order reaction which may be justified by the excess of hydrogen [63].

5. Conclusions

Several LDHs with chemical composition $(\text{Cu,Zn})_{1-x}\text{Al}_x(\text{OH})_2(\text{CO}_3)_{x/2} \cdot n\text{H}_2\text{O}$ have been synthesized by the co-precipitation method, maintaining a $(\text{Cu}^{2+} + \text{Zn}^{2+})/\text{Al}^{3+}$ molar ratio of 3, and varying the $\text{Cu}^{2+}/\text{Zn}^{2+}$ molar ratio between 0.2 and 6.0. After calcination and reduction steps, Cu/ZnO/Al₂O₃ catalysts were obtained. The physico-chemical characterization has revealed the formation of small Cu nanoparticles highly dispersed in the ZnO-Al₂O₃ structure.

All the catalysts were active in the gas-phase hydrogenation of furfural, with a high selectivity toward furfuryl alcohol, which is considered a valuable product due to its use for manufacturing resins. The presence of a low proportion of acid sites seems to disfavor consecutive reactions, being the formation of MF very limited in all cases. In addition, the textural properties of catalysts are typical of meso- and mainly macroporous solids, and the weaker Cu⁰-FUR interaction, in comparison to other

supports with stronger acidity, favors the lability of adsorbed reaction products and consequently shorter residence times, minimizing the deactivation by the formation of carbonaceous deposits.

In additional studies, the influence of the aging time in the synthesis of LDHs was also evaluated. The catalytic results have demonstrated that a shorter aging time leads to the formation of catalyst with a lower crystallinity, which favors the formation of Cu⁰-rich surfaces. This provides more active and stable catalysts, highly selective to FOL, obtaining a maximum FOL yield of 71% after 5 h of TOS at 210 °C for the CuZn_1 catalyst that was aged for 1 h.

Author Contributions: Conceptualization: J.A.C. and P.M.-T.; methodology: C.P.J.-G. and J.A.C.; validation: C.P.J.-G., J.A.C. and P.M.-T.; formal analysis: G.R.B. and C.P.J.-G.; investigation: G.R.B. and C.P.J.-G.; resources: P.M.-T.; data curation: C.P.J.-G. and J.A.C.; writing—original draft preparation: J.A.C.; writing—review and editing: C.P.J.-G., J.A.C. and P.M.-T.; visualization: C.P.J.-G. and J.A.C.; supervision: J.A.C. and P.M.-T.; project administration: P.M.-T.; funding acquisition: P.M.-T. All authors have read and agreed to the published version of the manuscript.

Funding: The authors are grateful to financial support from the Spanish Ministry of Innovation, Science and Universities (Project RTI2018- 094918-B-C44) and FEDER (European Union) funds.

Acknowledgments: J.A.C. and C.P.J.-G. thank University of Malaga for contracts of PhD incorporation.

Conflicts of Interest: The authors declare that they have no known competing financial interests or personal relationships that could have appeared to influence the work reported in this paper.

References

1. Cavanni, F.; Trifiró, F.; Vaccari, A. Hydrotalcite-type anionic clays: Preparation, properties and applications. *Catal. Today* **1991**, *11*, 173–301. [[CrossRef](#)]
2. Mishra, G.; Dash, B.; Pandey, S. Layered double hydroxides: A brief review from fundamentals to application as evolving biomaterials. *Appl. Clay Sci.* **2018**, *153*, 172–186. [[CrossRef](#)]
3. Bukhtiyarova, M.V. A review on effect of synthesis conditions on the formation of layered double hydroxides. *J. Solid State Chem.* **2019**, *269*, 494–506. [[CrossRef](#)]
4. Kuthati, Y.; Kankala, R.K.; Lee, C.H. Layered double hydroxide nanoparticles for biomedical applications: Current status and recent prospects. *Appl. Clay Sci.* **2015**, *112*, 100–116. [[CrossRef](#)]
5. Constantino, V.R.L.; Pinnavaia, T.J. Structure-reactivity relationships for basic catalysts derived from a Mg²⁺/Al³⁺/CO³⁻ layered double hydroxide. *Catal. Lett.* **1994**, *23*, 361–367. [[CrossRef](#)]
6. Prinetto, F.; Ghiotti, G.; Durand, R.; Tichit, D. Investigation of acid-base properties of catalysts obtained from layered double hydroxides. *J. Phys. Chem. B* **2000**, *104*, 11117–11126. [[CrossRef](#)]
7. Corma Canos, A.; Iborra, S.; Velty, A. Chemical routes for the transformation of biomass into chemicals. *Chem. Rev.* **2007**, *107*, 2411–2502. [[CrossRef](#)]
8. Climent, M.J.; Corma, A.; Iborra, S. Conversion of biomass platform molecules into fuel additives and liquid hydrocarbon fuels. *Green Chem.* **2014**, *16*, 516–547. [[CrossRef](#)]
9. Binder, J.B.; Raines, R.T. Simple chemical transformation of lignocellulosic biomass into furans for fuels and chemicals. *J. Am. Chem. Soc.* **2009**, *131*, 1979–1985. [[CrossRef](#)]
10. Alonso, D.M.; Wettstein, S.G.; Mellmer, M.A.; Gurbuz, E.I.; Dumesic, J.A. Integrated conversion of hemicellulose and cellulose from lignocellulosic biomass. *Energy Environ. Sci.* **2013**, *6*, 76–80. [[CrossRef](#)]
11. Delbecq, F.; Wang, Y.; Muralidhara, A.; El Ouardi, K.E.; Marlair, G.; Len, C. Hydrolysis of hemicellulose and derivatives—a review of recent advances in the production of furfural. *Front. Chem.* **2018**, *6*, 146–175. [[CrossRef](#)]
12. Mariscal, R.; Maireles-Torres, P.; Ojeda, M.; Sádaba, I.; López Granados, M. Furfural: A renewable and versatile platform molecule for the synthesis of chemicals and fuels. *Energy Environ. Sci.* **2016**, *9*, 1144–1189. [[CrossRef](#)]
13. Fúnez-Núñez, I.; García-Sancho, C.; Cecilia, J.A.; Moreno-Tost, R.; Pérez-Inestrosa, E.; Serrano-Cantador, L.; Maireles-Torres, P. Synergistic effect between CaCl₂ and γ-Al₂O₃ for furfural production by dehydration of hemicellulosic carbohydrates. *Appl. Catal. A Gen.* **2019**, *585*, 117188. [[CrossRef](#)]
14. Zeitsch, K.J. *The Chemistry and Technology of Furfural and Its Many By-Products*; Elsevier Science: New York, NY, USA, 2000.

15. Yan, K.; Wu, G.; Lafleur, T.; Jarvis, C. Production, properties and catalytic hydrogenation of furfural to fuel additives and value-added chemicals. *Renew. Sustain. Energy Rev.* **2014**, *38*, 663–676. [[CrossRef](#)]
16. Ramesh, D.; Reddy, T.S.; Narasimhulu, M.; Rajaram, S.; Suryakiran, N.; Mahesh, K.C.; Venkateswarlu, Y. Efficient and rapid stereoselective synthesis of trans-4,5-diaminocyclopent-2-enones by acidic ionic liquid under solvent-free conditions. *Chem. Lett* **2009**, *38*, 586–587. [[CrossRef](#)]
17. Nardi, M.; Costanzo, P.; de Nino, A.; di Gioia, M.L.; Olivito, F.; Sindona, G.; Procopio, A. Water excellent solvent for the synthesis of bifunctionalized cyclopentenones from furfural. *Green Chem.* **2017**, *19*, 5403–5411. [[CrossRef](#)]
18. Guo, J.; Xu, G.; Han, Z.; Zhang, Y.; Fu, Y.; Guo, Q. Selective conversion of furfural to cyclopentanone with CuZnAl catalysts. *ACS Sustain. Chem. Eng.* **2014**, *2*, 2259–2266. [[CrossRef](#)]
19. Li, S.W.; Batey, R.A. Mild lanthanide(III) catalyzed formation of 4,5-diaminocyclopent-2-enones from 2-furaldehyde and secondary amines: A domino condensation/ring-opening/electrocyclization process. *Chem. Commun.* **2007**, 3759–3761. [[CrossRef](#)]
20. Procopio, A.; Costanzo, P.; Curini, M.; Nardi, M.; Oliveira, M.; Sindona, G. Erbium(III) Chloride in ethyl lactate as a smart ecofriendly system for efficient and rapid stereoselective synthesis of trans-4,5-diaminocyclopent-2-enones. *ACS Sustain. Chem. Eng.* **2013**, *1*, 541–544. [[CrossRef](#)]
21. Burnett, L.W.; Johns, I.B.; Holdren, R.F.; Hixon, R.M. Production of 2-Methylfuran by Vapor-Phase Hydrogenation of Furfural. *Ind. Eng. Chem.* **1948**, *40*, 502–505. [[CrossRef](#)]
22. Manly, D.; Dunlop, A.P. Catalytic Hydrogenation. I. Kinetics and catalyst composition in the preparation of 2-methylfuran. *J. Org. Chem.* **1958**, *23*, 1093–1095. [[CrossRef](#)]
23. Seo, G.; Chon, H. Hydrogenation of furfural over copper-containing catalysts. *J. Catal.* **1981**, *67*, 424–429. [[CrossRef](#)]
24. Rao, R.; Dandekar, A.; Baker, R.T.K.; Vannice, M.A. Properties of Copper Chromite Catalysts in Hydrogenation Reactions. *J. Catal.* **1997**, *171*, 406–419. [[CrossRef](#)]
25. Nagaraja, B.M.; Siva Kumar, V.; Shasikala, V.; Padmasri, A.H.; Sreedhar, B.; David Raju, B.; Rama Rao, K.S. A highly efficient Cu/MgO catalyst for vapour phase hydrogenation of furfural to furfuryl alcohol. *Catal. Commun.* **2003**, *4*, 287–293. [[CrossRef](#)]
26. Nagaraja, B.M.; Padmasri, A.H.; David Raju, B.; Rama Rao, K.S. Vapor phase selective hydrogenation of furfural to furfuryl alcohol over Cu-MgO coprecipitated catalysts. *J. Mol. Catal. A Chem.* **2007**, *265*, 90–97. [[CrossRef](#)]
27. Sitthisa, S.; Sooknoi, T.; Ma, Y.; Balbuena, P.B.; Resasco, D.E. Kinetics and mechanism of hydrogenation of furfural on Cu/SiO₂ catalysts. *J. Catal.* **2011**, *277*, 1–13. [[CrossRef](#)]
28. Sitthisa, S.; Resasco, D.E. Hydrodeoxygenation of Furfural Over Supported Metal Catalysts: A Comparative Study of Cu, Pd and Ni. *Catal. Lett.* **2011**, *141*, 784–791. [[CrossRef](#)]
29. Dong, F.; Zhu, Y.; Zheng, H.; Zhu, Y.; Li, X.; Li, Y. Cr-free Cu-catalysts for the selective hydrogenation of biomass-derived furfural to 2-methylfuran: The synergistic effect of metal and acid sites. *J. Mol. Catal. A Chem.* **2015**, *398*, 140–148. [[CrossRef](#)]
30. Jiménez-Gómez, C.P.; Cecilia, J.A.; Durán-Martín, D.; Moreno-Tost, R.; Santamaría-González, J.; Mérida-Robles, J.; Mariscal, R.; Maireles-Torres, P. Gas-phase hydrogenation of furfural to furfuryl alcohol over Cu/ZnO catalysts. *J. Catal.* **2016**, *336*, 107–115. [[CrossRef](#)]
31. Ghashghae, M.; Sadjadi, S.; Shirvani, S.; Farzaneh, V. A Novel Consecutive Approach for the Preparation of Cu-MgO Catalysts with High Activity for Hydrogenation of Furfural to Furfuryl Alcohol. *Catal. Lett.* **2017**, *147*, 318–327. [[CrossRef](#)]
32. Jiménez-Gómez, C.P.; Cecilia, J.A.; Moreno-Tost, R.; Maireles-Torres, P. Selective Production of 2-Methylfuran by Gas-Phase Hydrogenation of Furfural on Copper Incorporated by Complexation in Mesoporous Silica Catalysts. *ChemSusChem* **2017**, *10*, 1448–1459. [[CrossRef](#)] [[PubMed](#)]
33. Jiménez-Gómez, C.P.; Cecilia, J.A.; Moreno-Tost, R.; Maireles-Torres, P. Selective Furfural Hydrogenation to Furfuryl Alcohol Using Cu-Based Catalysts Supported on Clay Minerals. *Top. Catal.* **2017**, *60*, 1040–1053. [[CrossRef](#)]
34. Yang, X.; Chen, H.; Meng, Q.; Zheng, H.; Zhu, Y.; Li, Y.W. Insights into influence of nanoparticle size and metal-support interactions of Cu/ZnO catalysts on activity for furfural hydrogenation. *Catal. Sci. Technol.* **2017**, *7*, 5625–5634. [[CrossRef](#)]

35. Sulmonetti, T.P.; Pang, S.H.; Claire, M.T.; Lee, S.; Cullen, D.A.; Agrawal, P.K.; Jones, C.W. Vapor phase hydrogenation of furfural over nickel mixed metal oxide catalysts derived from layered double hydroxides. *Appl. Catal. A Gen.* **2016**, *517*, 187–195. [[CrossRef](#)]
36. Manikandan, M.; Venugopal, A.K.; Prabu, K.; Jha, R.K.; Thirumalaiswamy, R. Role of surface synergistic effect on the performance of Ni-based hydrotalcite catalyst for highly efficient hydrogenation of furfural. *J. Mol. Catal. A Chem.* **2016**, *417*, 153–162. [[CrossRef](#)]
37. Guerrero-Torres, A.; Jiménez-Gómez, C.P.; Cecilia, J.A.; García-Sancho, C.; Quirante-Sánchez, J.J.; Mérida-Robles, J.M.; Maireles-Torres, P. Influence of the incorporation of basic or amphoteric oxides on the performance of Cu-based catalysts supported on sepiolite in furfural hydrogenation. *Catalysts* **2019**, *9*, 315. [[CrossRef](#)]
38. Nakagawa, Y.; Nakazawa, H.; Watanabe, H.; Tomishige, K. Total Hydrogenation of Furfural over a Silica-Supported Nickel Catalyst Prepared by the Reduction of a Nickel Nitrate Precursor. *ChemCatChem* **2012**, *4*, 1791–1797. [[CrossRef](#)]
39. Jiménez-Gómez, C.P.; Cecilia, J.A.; Moreno-Tost, R.; Maireles-Torres, P. Nickel Phosphide/Silica Catalysts for the Gas-Phase Hydrogenation of Furfural to High-Added-Value Chemicals. *ChemCatChem* **2017**, *9*, 2881–2889. [[CrossRef](#)]
40. Jiménez-Gómez, C.P.; Cecilia, J.A.; García-Sancho, C.; Moreno-Tost, R.; Maireles-Torres, P. Selective Production of Furan from Gas-Phase Furfural Decarbonylation on Ni-MgO Catalysts. *ACS Sustain. Chem. Eng.* **2019**, *7*, 7676–7685. [[CrossRef](#)]
41. Guerrero-Torres, A.; Jiménez-Gómez, C.P.; Cecilia, J.A.; García-Sancho, C.; Franco, F.; Quirante-Sánchez, J.J.; Maireles-Torres, P. Ni supported on sepiolite catalysts for the hydrogenation of furfural to value-added chemicals: Influence of the synthesis method on the catalytic performance. *Top. Catal.* **2019**, *62*, 535–550. [[CrossRef](#)]
42. Sitthisa, S.; Pham, T.; Prasomsri, T.; Sooknoi, T.; Mallinson, R.G.; Resasco, D.E. Conversion of furfural and 2-methylpentanal on Pd/SiO₂ and Pd-Cu/SiO₂ catalysts. *J. Catal.* **2011**, *280*, 17–27. [[CrossRef](#)]
43. Pino, N.; Sitthisa, S.; Tan, Q.; Souza, T.; López, D.; Resasco, D.E. Structure, activity, and selectivity of bimetallic Pd-Fe/SiO₂ and Pd-Fe/ γ -Al₂O₃ catalysts for the conversion of furfural. *J. Catal.* **2017**, *350*, 30–40. [[CrossRef](#)]
44. Yang, X.; Meng, Q.; Ding, G.; Wang, Y.; Chen, H.; Zhu, Y.L.; Li, Y.W. Construction of novel Cu/ZnO-Al₂O₃ composites for furfural hydrogenation: The role of Al components. *Appl. Catal. A Gen.* **2018**, *561*, 78–86. [[CrossRef](#)]
45. Nogueira, K.A.B.; Cecilia, J.A.; Santos, S.O.; Aguiar, J.E.; Vilarrasa-García, E.; Rodríguez-Castellón, E.; Azevedo, D.C.S.; Silva, I.J. Adsorption behavior of bovine serum albumin on Zn-Al and Mg-Al layered double hydroxides. *J. Sol-Gel Sci. Technol.* **2016**, *80*, 748–758. [[CrossRef](#)]
46. Santos, J.L.; Reina, T.R.; Ivanova, S.; Centeno, M.A.; Odriozola, J.A. Gold promoted Cu/ZnO/Al₂O₃ catalysts prepared from hydrotalcite precursors: Advanced materials for the WGS reaction. *Appl. Catal. B Environ.* **2017**, *201*, 310–317. [[CrossRef](#)]
47. He, L.; Cheng, H.; Liang, G.; Yu, Y.; Zhao, F. Effect of structure of CuO/ZnO/Al₂O₃ composites on catalytic performance for hydrogenation of fatty acid ester. *Appl. Catal. A Gen.* **2013**, *452*, 88–93. [[CrossRef](#)]
48. Fierro, J.L.G.; Melián-Cabrera, I.; López Granados, M. Reverse topotactic transformation of a Cu-Zn-Al catalyst during wet Pd impregnation: Relevance for the performance in methanol synthesis from CO₂/H₂ mixtures. *J. Catal.* **2002**, *210*, 273–284.
49. Chinchén, G.C.; Waugh, K.C.; Whan, D.A. The activity and state of the copper surface in methanol synthesis catalysts. *Appl. Catal.* **1986**, *25*, 101–107. [[CrossRef](#)]
50. Gervasini, A.; Bennici, S. Dispersion and surface states of copper catalysts by temperature-programmed-reduction of oxidized surfaces (s-TPR). *Appl. Catal. A Gen.* **2005**, *281*, 199–205. [[CrossRef](#)]
51. Yahiro, H.; Nakaya, K.; Yamamoto, T.; Saiki, K.; Yamaura, H. Effect of calcination temperature on the catalytic activity of copper supported on γ -alumina for the water-gas-shift reaction. *Catal. Commun.* **2006**, *7*, 228–231. [[CrossRef](#)]
52. Williamson, G.K.; Hall, W.H. X-ray line broadening line from filed aluminium and wolfram. *Acta Metall.* **1953**, *1*, 22–31. [[CrossRef](#)]
53. Studt, F.; Abild-Pedersen, F.; Varley, J.B.; Nørskov, J.K. CO and CO₂ hydrogenation to methanol calculated using the BEEF-vdW functional. *Catal. Lett.* **2013**, *143*, 71–73. [[CrossRef](#)]

54. Maderuelo-Solera, R.; López-Asensio, R.; Cecilia, J.A.; Jiménez-Gómez, C.P.; García-Sancho, C.; Moreno-Tost, R.; Maireles-Torres, P. Catalytic transfer hydrogenation of furfural to furfuryl alcohol over calcined MgFe hydrotalcites. *Appl. Clay Sci.* **2019**, *183*, 105351–105363. [CrossRef]
55. Thommes, M.; Kaneko, K.; Neimark, A.V.; Olivier, J.P.; Rodriguez-Reinoso, F.; Rouquerol, J.; Sing, K.S.W. Physisorption of gases, with special reference to the evaluation of surface area and pore size distribution (IUPAC Technical Report). *Pure Appl. Chem.* **2015**, *87*, 1051–1069. [CrossRef]
56. Landers, J.; Gor, G.Y.; Neimark, A.V. Density functional theory methods for characterization of porous materials. *Colloids Surfaces A Physicochem. Eng. Asp.* **2013**, *437*, 3–32.
57. Pakharukova, V.P.; Moroz, E.M.; Zyuzin, D.A.; Ishchenko, A.V.; Dolgikh, L.Y.; Strizhak, P.E. Structure of Copper Oxide Species Supported on Monoclinic Zirconia. *J. Phys. Chem. C* **2015**, *119*, 28828–28835.
58. Arango-Díaz, A.; Cecilia, J.A.; Dos Santos-Gómez, L.; Marrero-López, D.; Losilla, E.R.; Jiménez-Jiménez, J.; Rodríguez-Castellón, E. Characterization and performance in preferential oxidation of CO of CuO-CeO₂ catalysts synthesized using polymethyl metacrylate (PMMA) as template. *Int. J. Hydrog. Energy* **2015**, *40*, 11254–11260.
59. Kattel, S.; Ramírez, P.J.; Chen, J.G.; Rodriguez, J.A.; Liu, P. Active sites for CO₂ hydrogenation to methanol on Cu/ZnO catalysts. *Science (80-)* **2017**, *355*, 1296–1299. [CrossRef]
60. Peplinski, B.; Unger, W.E.S.; Grohmann, I. Characterization of CuZnAl oxide catalysts in the precipitated, calcined and reduced state by means of XPS with the help of a finger-print data base. *Appl. Surf. Sci.* **1992**, *62*, 115–129. [CrossRef]
61. Moulder, J.F.; Stickle, W.F.; Sool, P.E.; Bombardieri, K.D. *Handbook of X-ray Photoelectron Spectroscopy*; Perkin-Elmer: Eden Prairie, NM, USA, 1992.
62. Liu, D.; Zemlyanov, D.; Wu, T.; Lobo-Lapidus, R.J.; Dumesic, J.A.; Miller, J.T.; Marshall, C.L. Deactivation mechanistic studies of copper chromite catalyst for selective hydrogenation of 2-furfuraldehyde. *J. Catal.* **2013**, *299*, 336–345. [CrossRef]
63. Jiménez-Gómez, C.P.; Cecilia, J.A.; Márquez-Rodríguez, I.; Moreno-Tost, R.; Santamaría-González, J.; Mérida-Robles, J.; Maireles-Torres, P. Gas-phase hydrogenation of furfural over Cu/CeO₂ catalysts. *Catal. Today* **2017**, *279*, 327–338. [CrossRef]
64. Wu, J.; Shen, Y.; Liu, C.; Wang, H.; Geng, C.; Zhang, Z. Vapor phase hydrogenation of furfural to furfuryl alcohol over environmentally friendly Cu-Ca/SiO₂ catalyst. *Catal. Commun.* **2005**, *6*, 633–637. [CrossRef]
65. Solinas, V.; Ferino, I. Microcalorimetric characterisation of acid-basic catalysts. *Catal. Today* **1998**, *41*, 179–189. [CrossRef]
66. Gervasini, A.; Auroux, A. Microcalorimetric investigation of the acidity and basicity of metal oxides. *J. Therm. Anal.* **1991**, *37*, 1737–1744. [CrossRef]
67. Watanabe, K.; Yamagiwa, N.; Torisawa, Y. Cyclopentyl methyl ether as a new and alternative process solvent. *Org. Process Res. Dev.* **2007**, *11*, 251–258. [CrossRef]
68. Shi, Y.; Zhu, Y.; Yang, Y.; Li, Y.W.; Jiao, H. Exploring Furfural Catalytic Conversion on Cu(111) from Computation. *ACS Catal.* **2015**, *5*, 4020–4032. [CrossRef]
69. Pillai, U.R.; Deevi, S. Copper-zinc oxide and ceria promoted copper-zinc oxide as highly active catalysts for low temperature oxidation of carbon monoxide. *Appl. Catal. B Environ.* **2006**, *65*, 110–117. [CrossRef]
70. Jiménez-Gómez, C.P.; Cecilia, J.A.; Franco-Duro, F.I.; Pozo, M.; Moreno-Tost, R.; Maireles-Torres, P. Promotion effect of Ce or Zn oxides for improving furfuryl alcohol yield in the furfural hydrogenation using inexpensive Cu-based catalysts. *Mol. Catal.* **2018**, *455*, 121–131. [CrossRef]
71. Abderrazek, K.; Frini Srasra, N.; Srasra, E. Synthesis and Characterization of [Zn-Al] Layered Double Hydroxides: Effect of the Operating Parameters. *J. Chin. Chem. Soc.* **2017**, *64*, 346–353. [CrossRef]
72. Brunauer, S.; Emmett, P.H.; Teller, E. Adsorption of Gases in Multimolecular Layers. *J. Am. Chem. Soc.* **1938**, *60*, 309–319. [CrossRef]

